CURVATURE DETECTION AND SEGMENTATION OF RETINAL EXUDATES

Ivo Soares[1]*, Miguel Castelo-Branco*[1]*, António M.G. Pinheiro*[2]

[1]CICS - Centro de Investigação em Ciências da Saúde, University of Beira Interior, Covilhã, Portugal
[2]Unidade de Deteção Remota, University of Beira Interior, Covilhã, Portugal

ABSTRACT

In this paper, a segmentation method of the retinal images exudates is proposed. First, pixels that belong to exudates are located using the scale-space extrinsic curvature. These candidate points, are used together with the mean curvature to select possible exudates patches. True exudates are selected using the local maxima blob response through dynamical threshold, which will represent the final segmentation. The proposed scheme is tested with a retinal images public database. The ROC curve is used to validate the final performance, which shows a normalized area under the curve of 96.39%, with a confidence level of 0.8. In that case the sensitivity is 97.07%, the specificity is 99.90% and the accuracy is 99.83%. A final comparison with recent methods is also presented.

***Index Terms*—** Curvature, Scale-Space, Segmentation, Exudates, Retinal Image.

1. INTRODUCTION

Diabetic retinopathy is the main cause of blindness in diabetes. It is associated with the appearance of yellow spots in the retina, namely, hard and soft exudates. Hard exudates are yellow lipid sediments of serous leakage from damaged capillaries, and soft exudates are superficial retinal infarcts. They both appear as yellowish lesions, spread over the retina, with different sizes, shapes and brightness [1]. The fuzzy appearance of soft exudates is the only visible difference to the hard exudates. These characteristics make the exact detection and marking of exudates a true challenging task. A reliable detection and marking of these lesions makes possible an early detection of the disease, providing an invaluable help in screenings and follow-ups studies. A considerable number of papers have been published in recent years dealing with the detection of exudates. A complete comparative analysis of the most recent techniques is made on [2]. Recently, contextual information was used with computer-aided detection systems. The context is based on the spatial relation with surrounding anatomical landmarks, and similar lesions [3]. Mathematical morphologic methods were used by [4] and Neural Networks were used by [5]. In [6], exudates were detected without supervised learning steps. Using the seminal work in scale-space [7], a considerable attention was given to the application of scale-space analysis in ocular fundus images and on the detection of their distinct features, like retinal vessels and optic disk detection [8]. The extrinsic curvature was also applied for the detection of retinal features, like microaneurysms [9] and vessels [10]. In this paper, an algorithm for the detection and segmentation of exudates in retinal images is introduced. It is divided in two main parts; The first part deals with the computation of exudate locations, using an approximation of the extrinsic curvature, called Surface Tangent Derivative(STD) [9], in a scale-space framework. The second part performs the segmentation of the exudates through the mean curvature and the previously determined exudate locations. As will be discussed in the rest of the paper the curvature deals better with non-uniform illumination and contrast variation effects than the image intensity.

2. PROPOSED METHOD

The proposed method consists of two main processing steps:

1) Detection of the exudates locations.
2) Exudates segmentation.

2.1. Detection of the exudates locations

The candidate exudates locations are extracted from the images using a previously developed technique that is briefly described next [11]. The green channel component $I_G(x, y)$ of each RGB retinal fundus image is selected, since it offers the best contrast and provides the most relevant clinical visual information [1]. Using the definitions of the linear scale-space image representation [7], a family of derived images is defined by the convolution of $I_G(x, y)$ with the Gaussian filter $g(x, y, t)$, given by $L(x, y, t) = g(x, y, t) * I_G(x, y)$, $\forall t$, where $g(x, y, t) = \frac{1}{\sqrt{2\pi t}} e^{-\frac{(x^2+y^2)}{2t}}$. $2t$ is the variance of the Gaussian filter, which defines the scale level. Larger t values, result in stronger smoothing of $I_G(x, y)$, removing the details that are significantly smaller than t [7]. Although exudates can develop any shape, when they appear they assume a similar Gaussian profile. Also, a special care is needed for the detection of close exudates because of the possible feature merging that can occur in larger scales. The Gaussian mask

must be effective in noise reduction and in feature preservation. Hence, the following mask was applied,

$$W = \frac{1}{16}\begin{bmatrix} 1 & 2 & 1 \\ 2 & 4 & 2 \\ 1 & 2 & 1 \end{bmatrix}.$$

W corresponds to a Gaussian kernel with a variance $\sigma^2 = \sqrt{2}/2$. Since $\sigma^2 = 2t$, the parameter t can be defined at N different scales according to $t_n = n\frac{\sqrt{2}}{4}, n \in \{0, 1, ..., N-1\}$. The Gaussian scale-space representation is defined as $L(x, y, t_n)$, $n \in \{0, 1, ..., N-1\}$. After the scale-space definition, the scale-space curvature extremes detection is performed. The extrinsic curvature for a $1D$ function is given by, $k(x) = \frac{d\theta}{dl} = \frac{\frac{d\theta}{dx}}{\sqrt{1+\frac{dy^2}{dx^2}}}$. θ is the angle between the tangent at any point in the image surface and the x-axis. Considering only the numerator of $k(x)$, the Surface Tangent Derivative (STD) is given by $\gamma(x) = \frac{d\theta}{dx} = \frac{d}{dx}\arctan^{-1}(\frac{dy}{dx})$ [9]. $\gamma(x)$ also provides a measure of the rate of change of θ along a particular direction, and can be easily adapted in the detection of exudates locations. Hence, for any given scale t_n, $\gamma(x)$ is calculated in $L(x, y, t_n)$ in four specific directions $\alpha \in \{45°, 90°, 135°, 180°\}$, designated by $S_{t_n}(x, y, \alpha)$. Let tr_n be the curvature extremes threshold for the scale t_n, and $N(x, y)$ the 8 neighbourhood at any location (x, y). For each pixel location (x, y), the procedure to compute the scale-space extremes is described in Figure 1,

1. Evaluation of $|S_{max}(x, y)| = max\{S_{t_n}(x, y, \alpha)\}$, and the corresponding maximum orientation α_{max}.

$$M(x,y) = \begin{cases} 1, \begin{cases} \text{if } |S_{max}(x,y)| > tr_n \text{ and} \\ S_{t_n}(x,y,\alpha_{max}) < 0 \text{ and} \\ |S_{max}(x,y)| \geq S(N(x,y),\alpha_{max}) \end{cases} \\ 0, \text{otherwise} \end{cases}$$

Fig. 1. Curvature extremes computation

$M(x, y, t_n)$ is a binary image matrix that represents the thresholded scale-space curvature extremes locations. Each scale has its correspondent threshold tr_n, being dynamically computed. For each scale, the values $|S_{max}(x, y)|$ computed in step 1 in the algorithm of Figure 1 are saved in a vector $K(x, t_n)$. Figure 2 represents the outlines for $K(x, t_n)$ in ascending order. There is a value where each outline bends more sharply. This value divides the features with high curvature extremes from features with low curvature extremes values, making it ideal to be chosen as the threshold. As an example and considering Figure 2, for the scale t_0, the threshold tr_0 is determined at the point where the angle β, formed by the tangent vector at x, v_t, and the vector parallel to the x-axis, v_x, equals $\frac{\pi}{4}$. This process is repeated for every scale t_n. Finally, a coarse-to-fine scale pixel tracking is performed along the scale-space matrices, $M(x, y, t_n)$ [11]. The final locations are selected in the scale t_0, since it is the one closest to the initial image, providing a more accurate marking. A binary image results, where the white points are the candidates exudate locations, designated by $SD(x, y)$.

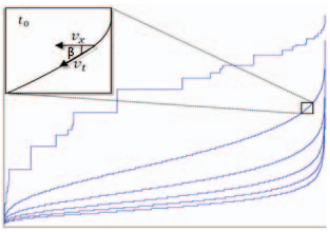

Fig. 2. Representation of $K(x, t_n)$ for all scales t_n in ascending order. The top outline represents the curvatures of the original image. The following outlines show the curvatures in the successive scales. The upper left image represents the calculation of the threshold for the scale t_o.

2.2. Exudates segmentation

The Hessian is a matrix of the second order partial derivatives that describes the local curvature of a function [12]. Considering $L = L(x, y, t_n)$, for any given scale t_n, the Hessian matrix can be written as,

$$H = \begin{bmatrix} L_{xx} & L_{xy} \\ L_{yx} & L_{yy} \end{bmatrix}. \quad (1)$$

The eigenvalues of the Hessian are found by solving the characteristic equation $|H - \lambda I| = 0$ relatively to λ, where I is the identity matrix, resulting in:

$$\lambda_1 = \frac{1}{2}\left(-\sqrt{2L_{xx}L_{yy} + L_{xx}^2 + 4L_{xy}^2 + L_{xx}^2} + L_{xx} + L_{yy}\right) \quad (2)$$

$$\lambda_2 = \frac{1}{2}\left(\sqrt{2L_{xx}L_{yy} + L_{xx}^2 + 4L_{xy}^2 + L_{xx}^2} + L_{xx} + L_{yy}\right). \quad (3)$$

λ_1 and λ_2 are the principal curvatures and represent the minimal and maximal curvatures at each point $p \in L$ respectively [12]. The mean curvature at p is the average of the principal curvatures,

$$MK = \frac{\lambda_1 + \lambda_2}{2}. \quad (4)$$

Figure 3 shows the comparison between an intensity profile and the mean curvature profiles at several scales, considering the same row. In the intensity profile, the effects of non-uniform illumination and contrast variation are well observed. However, in the mean curvature profiles, these effects almost disappear, revealing MK uniformization along the scales. It is also visible the presence of noise effects or small artefacts in the lower scales of the mean curvature profiles. Furthermore, Figure 3 b) shows that exudates belong to dark regions, and that they can be selected with an appropriate threshold. Hence, the curvature representation is used for image segmentation instead of the intensity. In order to avoid the noise

(a) Green channel

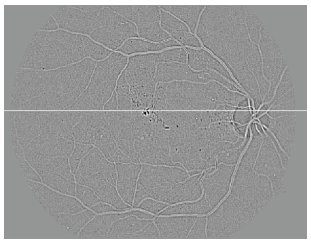

(b) Mean curvature image at scale t_4

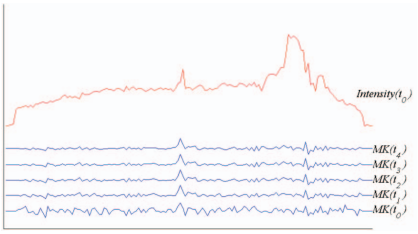

(c) Intensity and mean curvature variation for growing scales of the marked row

Fig. 3. Mean Curvature scale-space uniformization.

effects present in the lower scales, and the excessive blurring in larger scales, the segmentation is performed in a middle scale, t_s. After an normalization between 0 and 1, followed by an histogram equalization of the MK image at the scale t_s, $MK^{(he)}$, is computed. An initial segmentation is achieved by selecting all the pixels in $MK^{(he)}$ with values equal to zero, given by,

$$IS = \begin{cases} 1, & \text{if } MK^{(he)}(x,y) = 0. \\ 0, & \text{otherwise} \end{cases} \quad (5)$$

IS is a binary image where white patches represent exudate candidates. This segmentation is improved considering only the patches where at least one point of the SD image is present. After this step, because there are some regions with high curvature values that do not belong to exudates, few artefacts remain in the segmented image. Since exudates have a hill resemblance, they must have a high response to a blob detector, and can be selected using an appropriate threshold c. For the scale t_s, a blob detector can be defined as [12],

$$B = L_{xx}L_{yy} - L_{xy}^2. \quad (6)$$

For each patch in IS, the local maxima blob response is computed using eq. 6. These maxima responses are saved in a vector V_M. It was found, after extensive testing that the median of V_M is a good value for the threshold c. Hence, the final segmentation is achieved selecting only the patches that have a local maxima blob response larger than c (Figure 3).

3. RESULTS

The DIARETDB1 data base with 89 color retinal fundus images with size 1500x1152 was used for testing and performance evaluation (46 abnormal/43 normal). Ground truth images are provided for all images in the database both for hard and soft exudates [13]. These ground truth images are the result of several markings made by experts for each retinal fundus image. The areas are marked with a confidence level that depends of the number of experts that marked it as exudates or not. The ground truth images of both hard and soft exudates are merged, for each confidence level, since the method does not perform any separation between the two exudate types. The optic disk was manually removed from all the images. The proposed method depends on several parameters. Table 1 shows these parameters, the corresponding simulation set and the values that provide the best segmentation performance. The developed method reliability is based on the selection of the threshold values tr_n, that separate the curvatures extremes that are considered as valid exudates detections from the rejected ones. To study how the variation of these thresholds can influence the performance of the segmentation, they have been grown in steps. For each step, the number of extremes was grown 5% in each scale by selecting a new threshold value. The performance of the proposed method was evaluated on a pixel by pixel basis for each image. A pixel is considered: a true positive (TP) if it is contained in the ground truth labelled regions, a false negative (FN) if there is no pixel marking in the ground truth labelled region, a false positive (FP) if the pixel is marked in a ground truth region where no label exists, and a true negative (TN) if no marking appears in a non labelled region in the ground truth image. For each confidence level and for each step in the threshold value, the global sensitivity is computed for each image as $SE = TP/(TP + FN)$, and then averaged for the 89 images. The global specificity (SP) is computed in a similar way by employing $SP = TN/(TN + FP)$. Figure 3 represents several Receiver Operating Characteristic (ROC) curves. The best result is achieved for a confidence level of 1.0. However, when compared with the curve of confidence level of 0.8 there is no meaningful difference. Hence, the best sensitivity and specificity are respectively, 97.07% and 99.90% for a confidence level of 0.8. Table 2 shows the results achieved with the proposed method and a comparison with recent published methods.

Table 1. Method parameters.

Variable	Simulation set	Best performance
Size of W	$(3 \times 3), (5 \times 5), (7 \times 7)$	(3×3)
Number N	$\{0, 1, ..., 16\}$	6
scale t_s	$s \in \{0, 1, ..., 16\}$	4
threshold c	$mean, median, OTSU$	$median$

4. DISCUSSION AND CONCLUSIONS

In this paper a method that effectively deals with non-uniform illumination and contrast variation in retinal fundus images was proposed. This is achieved without any pre-processing

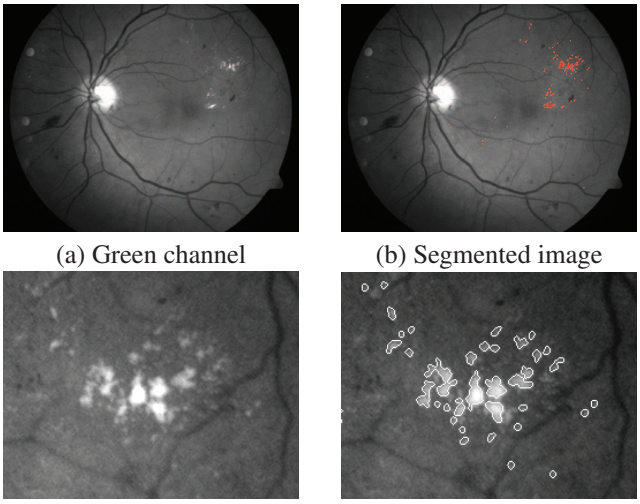

(a) Green channel (b) Segmented image

(c) Detailed green channel (d) Detailed segmented image

Fig. 4. Segmentation results

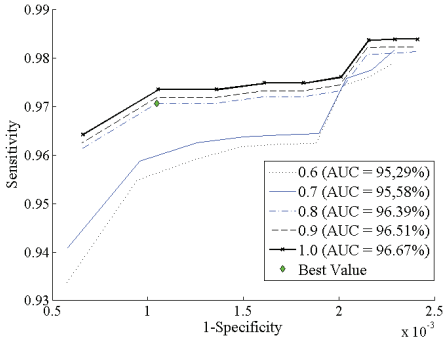

Fig. 5. ROC curve for exudates segmentation. Each curve represents a different confidence level with the respective Area Under the Curve (AUC).

steps, but rather considering the curvature space to perform the segmentation. The developed method exhibits a good performance, achieving results in line with the most recent techniques. This method reliability is provided by its dynamic structure, based on the scale-space analysis and dynamic thresholding. These results encourage future studies with a larger database. Moreover, an exudates classification method guided by this detection method is under development, in order to deal with the few artefacts that slightly reduce the performance.

5. REFERENCES

[1] R.J. Winder, P.J. Morrow, I.N. McRitchie, J.R. Bailie, and P.M. Hart, "Algorithms for digital image processing in diabetic retinopathy," *Computerized Medical Imaging and Graphics*, vol. 33, no. 8, pp. 608 – 622, 2009.

[2] A. Sopharak, B. Uyyanonvara, S. Barman, and T. Williamson, "Comparative analysis of automatic exudate detection algorithms," *WCE'10, London, U.K.*, pp. 738–741, 2010.

Table 2. Comparison of exudates segmentation methods.

Reference (using DIARETDB1)	Se %	Sp %	Acc %	Ni
Our method	97.07	99.9	99.83	89
Welfer [4]	70.48	98.84	—	47
Niemeijer [14]*	95.0	86.0	—	300
Garcia [5]*	88.14	92.6	97	67
Ravishankar [15]*	94.16	91.1	—	516

Se-Sensitivity, Sp-Specificity, Acc-Accuracy, Ni-Number of images. *-Uses a different database

[3] C.I. Sanchez, M. Niemeijer, M.S.A. Suttorp Schulten, M. Abramoff, and B. Van Ginneken, "Improving hard exudate detection in retinal images through a combination of local and contextual information," *ISBI'10*, pp. 5–8, 2010.

[4] D. Welfer, J. Scharcanski, and D.R. Marinho, "A coarse-to-fine strategy for automatically detecting exudates in color eye fundus images.," *Computerized medical imaging and graphics*, vol. 34, no. 3, pp. 228–235, 2010.

[5] M. García, C.I. Sánchez, A. Díez, M.I. López, and R. Hornero, "Detection of hard exudates based on neural networks as a diagnostic aid in the screening for diabetic retinopathy," *Telemedicine in Future Health*, 2006.

[6] L. Giancardo, F. Meriaudeau, T.P. Karnowski, Y. Li, K.W. Tobin, and E. Chaum, "Automatic retina exudates segmentation without a manually labelled training set.," *ISBI'11*, pp. 1396–1400, 2011.

[7] A.P. Witkin, "Scale-space filtering," *IJCAI'83*, vol. 2, pp. 1019–1022, 1983.

[8] C. Duanggate et. al, "Automatic optic disc detection for rop images using scale-space theory," *ICESIT 2010*, p. 64, 2010.

[9] J. Sivaswamy, G.D. Joshi, and S. Chandra, "An alternative curvature measure for topographic feature detection," *ICVGIP'06*, vol. 4338, pp. 228–239, 2006.

[10] S. Garg, J. Sivaswamy, and S. Chandra, "Unsupervised curvature-based retinal vessel segmentation," *ISBI'07*, pp. 344–347, 2007.

[11] I. Soares, M. Castelo-Branco, and A. M. G. Pinheiro, "Scale-space curvature detection of retinal exudates with a dynamic threshold," *ISPA'11*, pp. 523–528, 2011.

[12] Thomas Deserno, Ed., *Biological and Medical Physics, Biomedical Engineering*, Springer, 2011.

[13] T. Kauppi et. al, "The diaretdb1 diabetic retinopathy database and evaluation protocol," *Proc. MIUA'07*, pp. 61–65, 2007.

[14] M. Niemeijer, B. Van Ginneken, R. Stephen, M.S.A. Suttorp-Schulten, and M.D. Abràmoff, "Automated detection and differentiation of drusen, exudates, and cotton-wool spots in digital color fundus photographs for diabetic retinopathy diagnosis.," *Investigative Ophthalmology & Visual Science*, vol. 48, no. 5, pp. 2260–2267, 2007.

[15] S. Ravishankar, J.A. Ravishankar, and A. Mittal, "Automated feature extraction for early detection of diabetic retinopathy in fundus images," *IEEE CVPR'09*, pp. 210–217, 2009.